Multi-spectral photoacoustic elasticity tomography

Zhen Yuan, Yubin Liu

Zhen Yuan, Yubin Liu, "Multi-spectral photoacoustic elasticity tomography," Proc. SPIE 10494, Photons Plus Ultrasound: Imaging and Sensing 2018, 1049437 (19 February 2018); doi: 10.1117/12.2286797

SPIE.

Event: SPIE BiOS, 2018, San Francisco, California, United States

Photoacoustic elasticity tomography: Reconstruction algorithm, simulation and in vitro tests

Zhen Yuan， Yubin Liu

Bioimaging Core, Faculty of Health Sciences, University of Macau, Macau SAR, China
*zhenyuan@umac.mo

Abstract: The goal of this work was to develop and validate a spectrally resolved photoacoustic imaging method, namely multi-spectral photoacoustic elasticity tomography (PAET) for quantifying the physiological parameters and elastic modulus of biological tissues. We theoretically and experimentally examined the PAET imaging method using simulations and in vitro experimental tests. Our simulation and in vitro experimental results indicated that the reconstructions were quantitatively accurate in terms of sizes, the physiological and elastic properties of the targets.

Keywords: Photoacoustic imaging, multi-spectral imaging, elastic imaging

1. Introduction

Photoacoustic tomography (PAT) is a robust biomedical imaging method that can offer the structural and functional information of biological tissues with excellent resolution and high contrast [1-7]. PAT imaging techniques have been successfully applied to the early detection of cancer, probing the brain function and examining vascular and skin diseases [8-11]. More importantly, recent work also shows that PAT can reconstruct the tissue mechanical properties including the acoustic velocity, the elastic modulus and the temperature [12-15], and optical and physiological properties such as the optical absorption and scattering coefficients, the deoxyhemoglobin (HbR) and oxyhemoglobin (HbO2) concentrations by using spectrally resolved photoacoustic (PA) measurements [6,16-19]. In particular, the uniqueness regarding simultaneous reconstruction of different chromophore concentrations and acoustic velocity has been resolved for multi-spectral PAT [18], which can reveal spatially resolved quantitative physiological and molecular information by exploiting the known spectral characteristics of specific chromophores. The generated physiological properties of biological tissues including the concentrations of HbR and HbO2 and water (H2O) content are essential for an accurate diagnostic decision-making in lesion detection and image-guided cancer treatment.

Interestingly, the bulk elastic modulus of normal and diseased tissues have been explored by ultrasonography, where the ranges of the elastic moduli from soft tissues span over as much as four orders of the magnitudes [20,21]. Recently, PAT has been implemented to characterize the elastic moduli of phantoms or biological tissues using single-wavelength measurements. However, most of work conducted can only reconstruct the elastic moduli-related parameters, which can not achieve the truly quantitative and spectrally resolved PA elasticity tomography (PAET) [14]. In this study, multi-spectral PAET is proposed to directly reconstruct the chromophore concentrations and quantitative elastic modulus of biological tissues simultaneously. The capability of reconstructing the physiology and elastic properties by using multi-spectral PAET, paves a new avenue for better differentiating benign from

Photons Plus Ultrasound: Imaging and Sensing 2018, edited by Alexander A. Oraevsky, Lihong V. Wang, Proc. of SPIE Vol. 10494, 1049437 · © 2018 SPIE · CCC code: 1605-7422/18/$18 · doi: 10.1117/12.2286797

malignant lesions since the elastic contrast between diseased and healthy tissues is very high [21].

2. Methods and materials

2.1 The multi-spectral PAET reconstruction method

To formulate the reconstruction model for multi-spectral PAET, the PA wave generation and propagation in an acoustic coupling media are described by the basic Newton's law of motion Eq.(1), equation of continuity (2) and the thermal elastic equation (3) in terms of thermal confinement [1],

$$\rho(r)\frac{\partial}{\partial t}V(r,t) = -\nabla p(r,t). \tag{1}$$

$$\nabla \cdot V(r,t) = -\frac{1}{\rho(r)v_s^2(r)}\frac{\partial}{\partial t}p(r,t) + \beta\frac{\partial}{\partial t}T(r,t). \tag{2}$$

$$\rho(r)C_p\frac{\partial}{\partial t}T(r,t) = H(r,t). \tag{3}$$

where V is particle velocity, v_s is the acoustic velocity, t is time, r is the spatial location, ρ is the density of the media, T and p are the temperature and pressure, H is the source term which can be written as $H = \Psi I(t)$, C_p is the specific heat, Ψ is the light absorbed energy density, and $I(t)$ is the temporal illumination function. Considering Eqs. (1)-(3) and eliminating V, we get

$$\rho(r)\nabla\cdot(\frac{1}{\rho(r)}\nabla p(r,t)) - \frac{1}{v_s^2(r)}\frac{\partial^2}{\partial t^2}p(r,t) = -\frac{\beta}{C_p}\frac{\partial}{\partial t}H(r,t). \tag{4}$$

If the bulk elastic modulus K is denoted as $K = \rho v_s^2$, Eq. (4) is written,

$$\nabla(\frac{1}{\rho(r)}\nabla p(r,t)) - \frac{1}{K}\frac{\partial^2}{\partial t^2}p(r,t) = -\frac{\beta}{\rho C_p}\frac{\partial}{\partial t}H(r,t). \tag{5}$$

If a homogeneous elastic reference medium is assumed with density $\rho = \rho_0$, Eq. (5) is written,

$$\nabla^2 p(r,t) - \frac{\rho_0}{K}\frac{\partial^2}{\partial t^2}p(r,t) = -\frac{\beta}{C_p}\frac{\partial}{\partial t}H(r,t). \tag{6}$$

Denoting the following Fourier transform form for acoustic pressure,

$$P(r,\omega) = \int_{-\infty}^{+\infty} p(r,t)\exp(-i\omega t)dt. \tag{7}$$

And taking the Fourier transform on variable t of Eq. (7), we obtain,

$$\nabla^2 p(r,\omega) + \frac{K_0}{K}k_0^2 p(r,\omega) = i\frac{k_0\beta}{C_p}v_0\Psi(r). \tag{8}$$

where $k_0 = \omega / v_0$ is the wave number described by the angular frequency ω and the speed of acoustic wave v_0 in a reference medium, K_0 is the bulk elastic modulus of the reference medium and the light absorbed energy density Ψ is equal to the product of the optical absorption coefficient μ_a and photon density Φ. Eq. (8) can be further written as

$$\nabla^2 p(r,\omega) + Ok_0^2 p(r,\omega) = i\frac{k_0\beta}{C_p}v_0\Psi(r). \tag{9}$$

where O is a coefficient that depends on the bulk modulus K and $O = K_0 / K$.

In multi-spectral PAT, the frequency-domain Helmholtz wave equation is expresses as

$$\nabla^2 p(r,\omega,\lambda) + Ok_0^2 p(r,\omega,\lambda) = i\frac{k_0\beta}{C_p} v_0 \mu_a(r,\lambda)\Phi(r,\lambda) \tag{10}$$

where λ is the wavelength of the incident light. According to the Beer's law, the wavelength-dependent tissue absorption coefficient is written [16,18],

$$\mu_a(\lambda) = \sum_{i=1} \varepsilon_i(\lambda) c_i . \tag{11}$$

in which c_i is the concentration and $\varepsilon_i(\lambda)$ is the extinction coefficient of the *i*th chromophore at wavelength λ. Consequently, Eq. (10) is rewritten,

$$\nabla^2 p(r,\omega,\lambda) + Ok_0^2 p(r,\omega,\lambda) = i\frac{k_0\beta}{C_p} v_0 \sum_{i=1} \varepsilon_i(\lambda) c_i \Phi(r,\lambda). \tag{12}$$

Eq. (12) is the forward equation for multi-spectral PAET and the finite element discretization form of Eq. (12) is [16,18],

$$\boldsymbol{Ap} = \boldsymbol{B} \tag{13}$$

The inverse solution can be obtained by solving the following inverse equation:

$$(\boldsymbol{J}^T\boldsymbol{J} + \xi\boldsymbol{I})\Delta\boldsymbol{\chi} = \boldsymbol{J}^T(\boldsymbol{p}^o - \boldsymbol{p}^c). \tag{14}$$

in which $\Delta\chi = \left(\Delta c_{l,1} \quad \Delta c_{l,2} \quad \ldots \quad \Delta c_{l,n} \quad \Delta O_1 \quad \Delta O_2 \quad \ldots \quad \Delta O_n\right)^T$ is the update vector for l chromophores, elasticity modulus-related parameter O and N is the node number of the finite element mesh; ξ is the regularization parameter determined by combined Marquardt and Tikhonov regularization schemes [16]; $\boldsymbol{p}_i^o$ and $\boldsymbol{p}_i^c$ are measured and calculated data for i=1,2,…M boundary locations and are written as for each acoustic frequency ω within each incident optical wavelength λ,

$$\boldsymbol{p}^o = (p_1^o, p_2^o, \cdots, p_M^o)^T \big|(\omega,\lambda), \quad \boldsymbol{p}^c = (p_1^c, p_2^c, \cdots, p_M^c)^T \big|(\omega,\lambda). \tag{15}$$

The Jacobian matrix, $\boldsymbol{J}$ is denoted as $\boldsymbol{J} = [\tilde{\boldsymbol{J}}_{O,\lambda,\omega}, \tilde{\boldsymbol{J}}_{c_i,\lambda,\omega}]$, where $\tilde{\boldsymbol{J}}_{O,\lambda,\omega}$ and $\tilde{\boldsymbol{J}}_{c_i,\lambda,\omega}$ represents the Jacobian submatrix for the elastic modulus and different chromophores, respectively [15]. In consideration of $\Psi = \mu_a\Phi$, the elements in Jacobian matrix $\tilde{\boldsymbol{J}}_{c_i,\lambda,\omega}$ are determined by

$$\frac{\partial p_i(\omega,\lambda)}{\partial (c_l)_j} = \sum_{k=1}^{N} \left(\frac{\partial p_i(\omega,\lambda)}{\partial \Psi_k(\lambda)} \frac{\partial \Psi_k(\lambda)}{\partial \mu_{a,j}(\lambda)} \varepsilon_l(\lambda)\right) \quad (i = 1,2...M; j = 1,2...N; l = 1,2...Chrom). \tag{16}$$

in which Chrom is the number of chromophores and the derivatives $\partial\Psi/\partial\mu_a$ in Eq. (3) are further denoted as

$$\frac{\partial \Psi_k(\lambda)}{\partial \mu_{aj}(\lambda)} = \begin{pmatrix} \Phi_j + \mu_{a,j}(\partial\Phi_j/\partial\mu_{a,j}) & if \quad (k=j) \\ \mu_{a,k}(\partial\Phi_k/\partial\mu_{a,j}) & if \quad (k\neq j) \end{pmatrix} \big|(\lambda). \tag{17}$$

The sensitivity of $\partial p(\omega,\lambda)/\partial\Psi(\lambda)$ and $\partial\Phi/\partial\mu_a$ in each iteration can be calculated from Eq. (10) and the following photon diffusion equation for each wavelength, respectively,

$$\nabla\cdot D(r,\lambda)\nabla\Phi(r,\lambda) - \mu_a(r,\lambda)\Phi(r,\lambda) = -S(r,\lambda). \tag{18}$$

in which *S(r)* is the light source term and *D(r)* is the optical diffusion coefficient and assumed as a constant in this study.

Likewise, the elements in Jacobian submatrix $\tilde{\boldsymbol{J}}_{O,\lambda,\omega}$ are determined by [22],

$$[A]\left\{\frac{\partial p(\omega,\lambda)}{\partial O_j}\right\} = -\left[\frac{\partial A}{\partial O_j}\right]\{p(\omega,\lambda)\}. \tag{19}$$

The Jacobian matrix can be calculated through the following steps using the adjoint method:

First, we define a MxN matrix Ψ , and let Ψ satisfy the following relationship:

$$[\Psi][A]=[\Delta_d]. \tag{20}$$

where the vector Δ_d has the unit value at the measurement sites/nodes and zero at other nodes. Then we left multiply Eq. (19) by Ψ , which yields

$$[\Psi][A]\left\{\frac{\partial p(\lambda)}{\partial O_j}\right\}=-[\Psi]\left[\frac{\partial A}{\partial O_j}\right]\{p(\lambda)\}. \tag{21}$$

Inspecting Eq. (20) into Eq. (21), we can immediately find that the left hand side of Eq. (21) actually gives the corresponding elements in the Jacobian submatrix $\tilde{\boldsymbol{J}}_{O,\lambda,\omega}$.

As such, in multi-spectral PAET, the image formation task is to update chromophores concentration and bulk elastic modulus distributions via the iterative solution of Eqs. (13), (14) and (18) so that a weighted sum of the squared difference between computed and measured acoustic pressures can be minimized.

2.2 The multi-spectral PAET imaging systems

For our home-made PAT imaging system at the Faculty of Health Sciences of the University of Macau, a pulsed light from an Nd:YAG laser with OPO based on the multi-wavelength excitation (wavelength range from 680 to 1064 nm; pulse duration: 5-10 ns; frequency rate: 20 Hz; Surelite I-10, Continuum) was used to illuminate the phantom/biological tissues via an optical subsystem and generated acoustic signals. A transducer (1MHz central frequency; OLYMPUS NDT) and the phantom were immersed into a water tank. A rotary stage rotated the transducer relative to the center of the tank as shown in Fig.1. The incident optical fluence was controlled at 10 mJ/cm^2, and the diameter of the incident laser beam was 2.0 cm. The complex wavefield signal was amplified by a Pulser/Receiver (5073R, OLYMPUS).

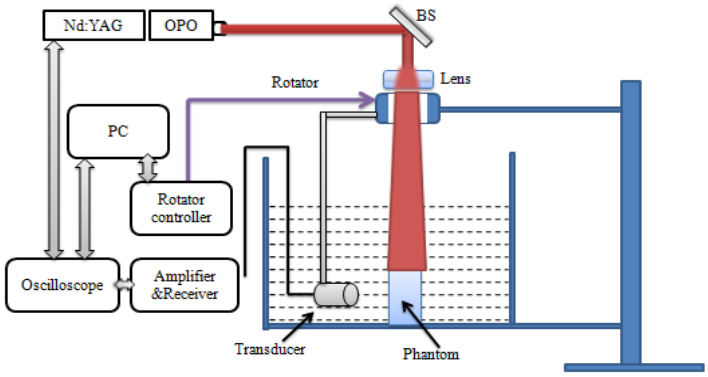

Fig.1. Schematic of the PAT system. BS: beam splitter; PC: personal computer.

2.3 Simulation and in vitro experimental tests

For simulation test 1, a circular background with the diameter of 3cm contained three circular targets (2mm in radius each as shown in Fig. 2(a)), where each target had different contrasts in physiological properties (Hb, HbO_2, and H_2O) and bulk elastic modulus (K). The chromophore concentrations and K used were provided in Table 1 and six optical wavelengths

(633, 670, 723, 805, 854and 896nm) were utilized to generate the measurements for the multi-spectral PAET. A total of 120 detectors were equally distributed along the boundary of the circular background. The extinction coefficient for each chromophore was adopted from the website at http://omlc.ogi.edu/spectra/index.html [23].

In addition, for the first in vitro experiment, we embedded a square chicken breast (length: 3mm; width:2mm) into a 3.5-cm-diameter solid cylindrical phantom. We then immersed the chicken breast-bearing solid phantom into the water tank. Two optical wavelengths (532 and 680nm) were used for the measurements. The phantom materials used consisted of Intralipid as scatterer and India ink as absorber with Agar powder (1-2%) for solidifying the Intralipid and India ink solution.

3. Results and discussion

In the following sections we show the reconstruction results that demonstrate the feasibility of the multi-spectral PAET reconstruction method. The multi-spectral PAET approach is examined using several simulations and in vitro experiments based on the reconstruction model and imaging systems mentioned above.

Fig. 2 showed the recovered results for simulation case 1, in which the figures on the left column of Fig. 2 displayed the exact locations of the targets including HbO_2, HbR, H_2O and K whereas the recovered images were presented in Figs. 2(b)-2(c) corresponding to HbO_2, HbR, H_2O and K, respectively. It was discovered from the recovered results in Fig. 2 that the crosstalk errors between the chromophore concentrations and bulk elastic modulus were effectively resolved by using our multi-spectral PAET reconstruction method.

Table 1. Chromophore Concentrations and *K* for the targets in simulation test 1

Objects position	HbO_2 (μM)	HbR (μM)	H_2O (%)	K (GPa)
Background	6	2	20	2.2
Top right	6	10	20	2.2
Top left	6	2	70	2.8
Bottom middle	20	2	20	2.8

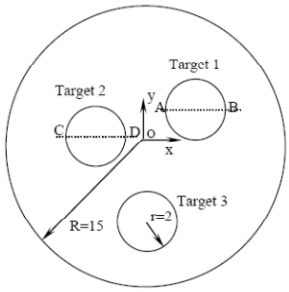

(a)

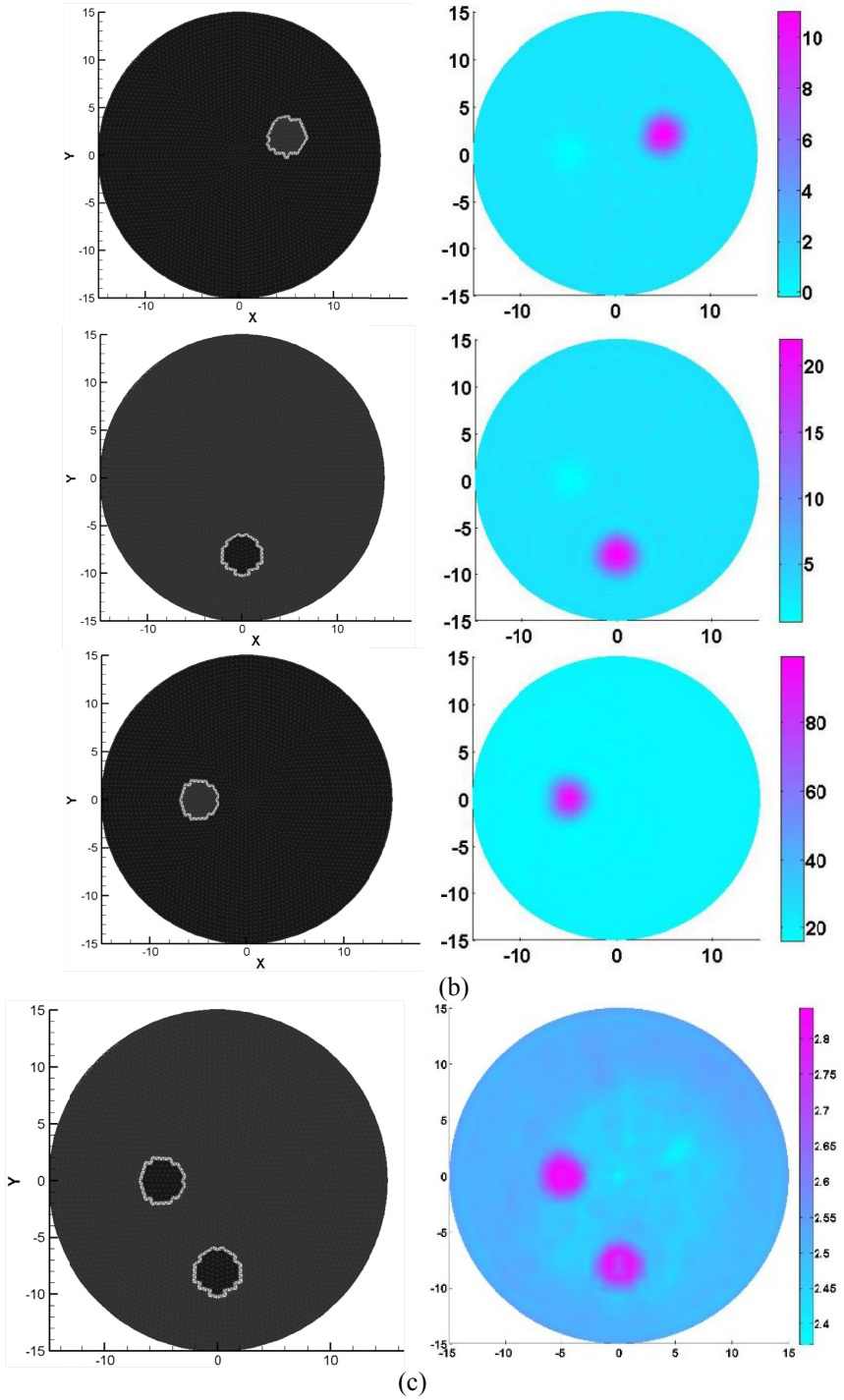

Fig. 2. (a) Test geometry. The dimension units are in millimeters. (b) and (c) show the exact (left column) and recovered (right column) images using 6 optical wavelengths. The first to the third rows of Fig. 2(b) denote the Hb, HBO_2 and H_2O, respectively whereas while 2(c) denotes K. The axes (left and bottom) illustrate the spatial scale, in mm, whereas the color scale (right) denote HbO_2 and HbR in μM, H_2O in percentage, and K in GPa.

The first in vitro test was performed to explore the merits of the developed multi-spectral PAET reconstruction method. For this experiment, we used the chicken breast as the target, as plotted in Fig. 3(a). The imaging results were provided in Fig.3, in which Figs. 3(b) and 3(c) showed the recovered HbR concentration and bulk elastic modulus K, respectively. Likewise, by estimating the full width half maximum of the quantitative properties profiles in Fig. 3, we found the reconstructed HbR concentration of the chicken breast was nearly 10 μM while the corresponding peak values of K was 2.5GPa. In particular, the reconstructed size of the chicken breast in length was 3.1mm, which was in good agreement with its true size of 3.0mm.

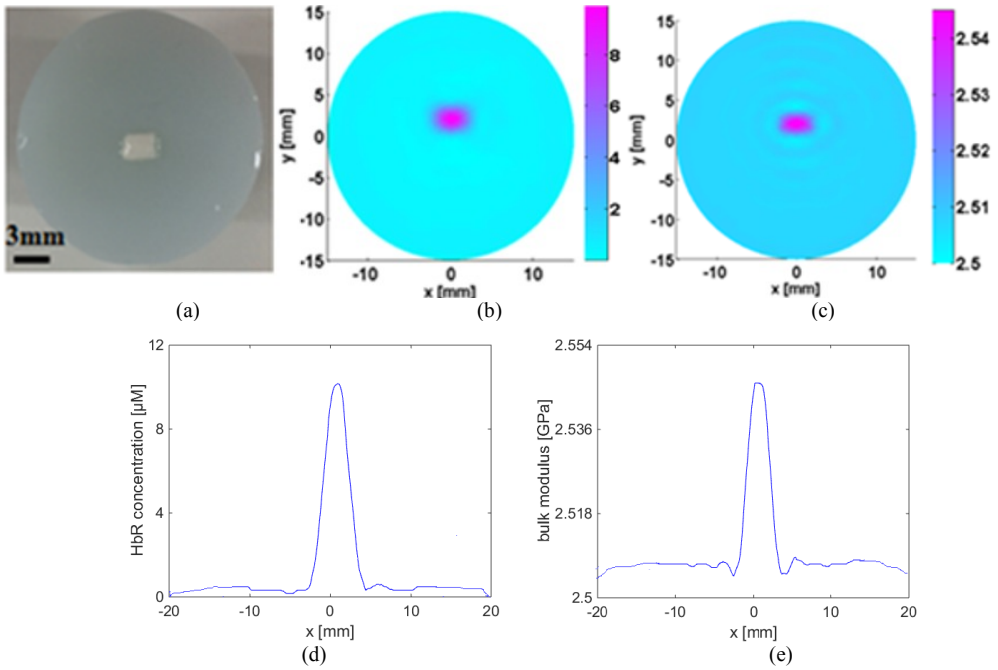

Fig. 4. The Photograph of the chicken breast used for the first in vitro experimental test (a), the recovered HbR concentration image (b), the recovered K image (c), the HbR profile plotted along the center of the target (d), and the K profile plotted along the center of the target (left) (e). The axes (left and bottom) illustrate the spatial scale, in mm, whereas the color scale (right) denote HbR in μM and K in GPa.

In summary, our reconstruction results indicated that quantification of chromophore concentrations and elastic bulk modulus is feasible by using the developed PAET imaging method when spectral priors are incorporated into the inverse reconstruction. In particular, images that are generated from simulated data and in vitro data are presented, in which both the physiological and K properties images can be reconstructed using our multi-spectral PAET reconstruction algorithm. The spectrally resolved PAET approach provides an efficient means of concurrent reconstruction of multiple parameters including different chromophore concentrations and K. More importantly, it is clear from the reconstructed results that the crosstalk issue for recovery of multiple parameters are successfully resolved by using multi-spectral PA measurements. Specifically, multi-spectral PAET can effectively minimize the crosstalk error and improve the image quality for all the test cases. In addition, we discovered that the PAET image reconstruction methods are also able to quantitatively reconstruct absorbing objects of different sizes and different elastic modulus contrast levels. Nonetheless, the ability of reconstructing the elastic property image by using PA measurements may

provide us a novel tool to quantify physiological function, disease progression, or response to intervention.

Acknowledgments

This study was supported by grants MYRG2014-00093-FHS, MYRG 2015-00036-FHS and MYRG2016-00110-FHS from the University of Macau in Macau and grants FDCT 026/2014/A1 and FDCT 025/2015/A1 from the Macao government.

References

1. L.V.Wang, H. Wu, Biomedical Optics: Principles and Imaging (Wiley, 2007).
2. G. Paltauf and H. Schmidt-Kloiber, "Pulsed optoacoustic characterization of layered media," J.Appl.Phys.**88**, 1624–1631(2000).
3. A.A. Oraevsky, S.L. Jacques, and F.K. Tittel, "Measurement of tissue optical properties by time-resolved detection of laser-induced transient stress,"Appl.Opt.**36**, 402–415(1997).
4. R. Zemp, "Quantitative photoacoustic tomography with multiple optical sources," Appl .Opt. **49**, 3566-72(2010).
5. J. Ripoll, V. Ntziachristos, "Quantitative point source photoacoustic inversion formulas for scattering and absorbing medium," Phys. Rev. E **71**, 031912 (2005).
6. B. Cox, S. Arridge, K. Kostli and P. Beard, "2D quantitative photoacoustic image reconstruction of absorption distributions in scattering medium using a simple iterative method," Appl. Opt. **45**, 1866-1875 (2006).
7. C. Xu, P. Kumavor, A. Aguirre, Q. Zhu, "Quantitative recovery of absorption coefficient using DOT-assisted photoacoustic tomography for breast imaging," BsuD in OSA Biomedical Optics Topical Meeting, Miami, FL, 2010.
8. S. Yang, D. Xing, Y. Lao, D. Yang, L. Zeng, "Noninvasive monitoring of traumatic brain injury and post-traumatic rehabilitation with laser-induced photoacoustic imaging," Applied Physics Letters **90**(24), 243902 (2007).
9. J. Oh, M. Li, H. Zhang, K. Maslov, G., L. Wang, "Three-dimensional imaging of skin melanoma in vivo by dual-wavelength photoacoustic microscopy," Journal of Biomedical Optics **11**(3), 034032 (2006).
10. A. Agarwal, S. Huang, M. O'donnell, K.C.Day, M. Day, N. Kotov, S. Ashkenazi, "Targeted gold nanorod contrast agent for prostate cancer detection by photoacoustic imaging," Journal of Applied Physics102(6), 064701 (2007).
11. X. Wang, W. Roberts, P. Carson, et al., "Photoacoustic tomography: a potential new tool for prostate cancer," Biomedical Optics Express **1**(4): 1117-1126 (2010).
12. Z. Yuan, Q. Zhang, H. Jiang, "Simultaneous reconstruction optical and acoustic properties by quantitative photoacoustic tomography," Optics Express **14**, 6749-6754 (2006).
13. J. Shah, S. Park, S. Aglyamov, T. Larson, L. Ma, K. Sokolov, K. Johnston, T. Milner, and S. Emelianoy, "Photoacoustic imaging and temperature measurement for photothermal cancer therapy," Journal of Biomedical Optics **13**(3), 034024(2008).
14. M.S. Singh, H. Jiang, "Elastic property attributes to photoacoustic signals: an experimental phantom study," Opt. Lett. **39**(13), 3870-3972(2014).
15. Z. Yuan, X. Li, L. Xi, "Listening to light scattering in turbid media: quantitative optical scattering imaging using photoacoustic measurements with one-wavelength illumination," Journal of Optics **065301**, 1-9 (2014).
16. Z. Yuan, H Jiang, "Quantitative photoacoustic tomography: recovery of optical absorption coefficient maps of heterogeneous medium," Applied Physics Letters **88**, 231101APL 1-3 (2006).
17. Y. Liu, H. Jiang, Z. Yuan, "Two-scheme for quantitative photoacoustic tomography based on Monte Carlo simulation," Med. Phys. **43**(7), 1-11(2016).
18. Z. Yuan, H. Jiang, "Simultaneous recovery of tissue physiological and acoustic properties and the criteria for wavelength selection in multi-spectral photoacoustic tomography," Optics Letters **34**, 1714-1716 (2009).
19. S Li, B Montcel, Z Yuan, W. Liu, D. Vray, "Multigrid-based reconstruction algorithm for quantitative photoacoustic tomography," Biomedical Optics Express **6**(7), 2424-2434 (2015).
20. F. A. Duck, Physical properties of tissues: a comprehensive reference book, Academic press, (2013).
21. T. Glozman, H. Azari, "A method for characterization of tissue elastic properties combining ultrasound computed tomography with elastography," J. Ultrasound Med. **29**, 387-398(2010).
22. H. Jiang, Z. Yuan, X. Gu, "Spatially varying optical and acoustic property reconstruction using finite element-based photoacoustic tomography," J. Opt. Soc. Am. A **23**, 878-888 (2006).
23. http//omlc.ogi.edu/spectra/index.html.
24. J. P. Ritz, A. Roggan, C. Isbert, G. Müller, H. J. Buhr, and C. T. Germer, "Optical properties of native and coagulated porcine liver tissue between 400 and 2400 nm," Lasers Surg. Med. **29**(3), 205–212 (2001)